ENVIRONMENT AND PROTOSTELLAR EVOLUTION

YICHEN ZHANG[1,2] AND JONATHAN C. TAN[3,4]
[1] Departamento de Astronomía, Universidad de Chile, Casilla 36-D, Santiago, Chile; yczhang.astro@gmail.com
[2] Department of Astronomy, Yale University, New Haven, CT 06520, USA
[3] Department of Astronomy, University of Florida, Gainesville, FL 32611, USA
[4] Department of Physics, University of Florida, Gainesville, FL 32611, USA

ABSTRACT

Even today in our Galaxy, stars form from gas cores in a variety of environments, which may affect the properties of the resulting star and planetary systems. Here, we study the role of pressure, parameterized via ambient clump mass surface density, on protostellar evolution and appearance, focusing on low-mass Sun-like stars and considering a range of conditions from relatively low pressure filaments in Taurus, to intermediate pressures of cluster-forming clumps like the Orion Nebula Cluster, to very high pressures that may be found in the densest infrared dark clouds or in the Galactic center. We present unified analytic and numerical models for the collapse of prestellar cores, accretion disks, protostellar evolution, and bipolar outflows, coupled with radiative transfer calculations and a simple astrochemical model to predict CO gas-phase abundances. Prestellar cores in high-pressure environments are smaller and denser and thus collapse with higher accretion rates and efficiencies, resulting in higher luminosity protostars with more powerful outflows. The protostellar envelope is heated to warmer temperatures, affecting infrared morphologies (and thus classification) and astrochemical processes like CO depletion onto dust grain ice mantles (and thus CO morphologies). These results have general implications for star and planet formation, especially via their effect on astrochemical and dust grain evolution during infall to and through protostellar accretion disks.

Key words: stars: formation

1. INTRODUCTION

In self-gravitating virialized gas clumps, the internal pressure is set by the gas envelope weight, which is related to the more easily observable mass surface density, Σ_{cl}, via $P \simeq G\Sigma_{cl}^2$ (McKee & Tan 2003, hereafter MT03). Observed Σs of star-forming regions vary greatly, from regions like Taurus with $\Sigma \sim 0.03$ g cm^{-2} (Onishi et al. 1996) where low-mass stars are forming in relative isolation, to regions like the Orion Nebula Cluster (ONC) with $\Sigma \sim 0.3$ g cm^{-2} (MT03) where low-mass stars are more crowded around massive stars. Infrared dark clouds (IRDCs) have $\Sigma \sim 0.1 - 1$ g cm^{-2} (Butler & Tan 2012). Some massive-star-forming regions reach $\Sigma \gtrsim 1$ g cm^{-2} (Plume et al. 1997; Battersby et al. 2014; Tan et al. 2014). Here low-mass stars are also expected to form along with massive stars from the fragmenting clump. The Galactic center (GC) region clouds, such as the "Brick," also contain clumps of very high Σ (Rathborne et al. 2014). How do these different environmental conditions affect the formation of Sun-like stars?

In the Turbulent Core model for massive star formation (MT03), the initial core size and subsequent protostellar evolution are determined using the initial core mass, M_c, and Σ of the surrounding clump. This model can be extended to low-mass star formation, assuming cores are approximately virialized and in pressure balance with the clump. A prestellar core, i.e., on the verge of collapse, of a given mass in a higher Σ environment experiences higher surface pressure, is therefore more compact and dense, and thus collapses with a higher accretion rate. Higher luminosity due to faster accretion and a more compact structure make the core warmer. Such a dependence of the protostellar core temperature on environment has further implications for infrared morphologies,

chemical evolution of the core and disk, and potentially planet formation.

The above scenario falls within the "core accretion" paradigm, in which the accretion rate and final stellar mass are determined by the initial conditions of the core. In the alternative "competitive accretion" paradigm (Bonnell et al. 2001), there is no such dependence on initial core properties.

Some observations of protoclusters suggest neighboring protostars have more correlated luminosities and accretion rates (Elmegreen et al. 2014; Kryukova et al. 2014). This has been explained by invoking mass segregation and large-scale accretion flows, which appear in competitive accretion, but may also result from an accretion rate dependence on the star formation environment as predicted by the core accretion. A better quantitative understanding of this environmental dependence will help solve this question.

Here we study how the star-forming environment (Σ_{cl}) affects thermal evolution, infrared morphologies, and CO gas-phase abundances of protostellar cores. The infrared appearance of low-mass protostars and its dependence on envelope, disk, and outflow properties were studied by Robitaille et al. (2006) with a suite of RT models. The temperature and chemical evolution of protostellar cores have also been studied using various astrochemistry models incorporated into either analytical models of collapse (e.g., Visser et al. 2009, 2011) or dynamical simulations (e.g., Hincelin et al. 2013). However, the dependence of temperature evolution, infrared morphology, and chemistry on initial environmental conditions, especially pressure and Σ, has not yet been studied with a self-consistent model including collapsing cores, disks, gradually widening outflow cavities, and full protostellar evolution. This is our goal.
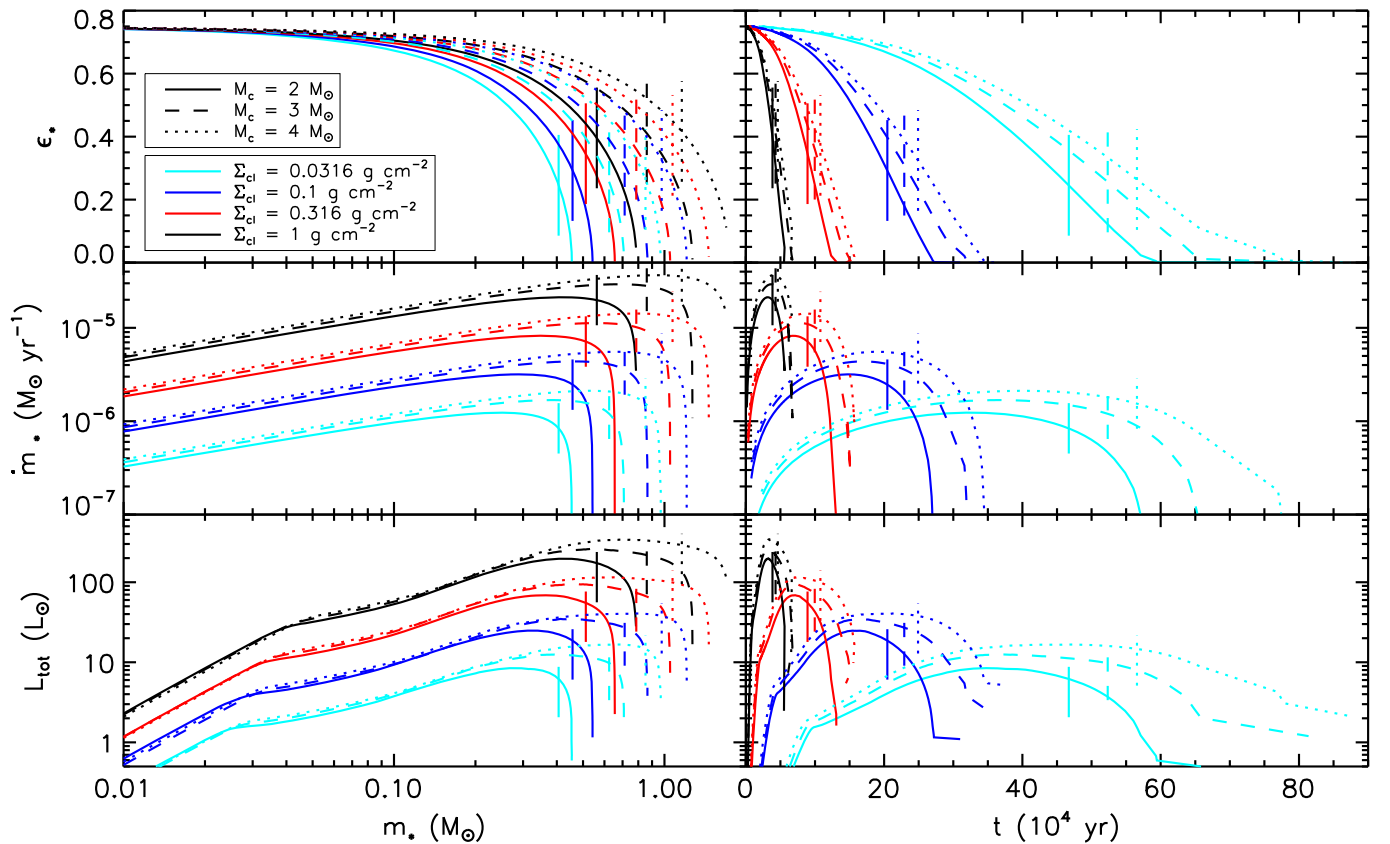
Figure 1. Evolution of star formation efficiency (top), stellar accretion rate (middle), and total luminosity (bottom) in models with various Σ_{cl} and M_c (see the legend) vs. stellar mass (left column) and time (right column). The short vertical lines indicate when $m_* = M_{env}$.

2. MODELS

In several papers (Zhang & Tan 2011; Zhang et al. 2013, 2014, hereafter ZT11, ZTM13, ZTH14), we have developed an RT model for massive star formation, following evolutionary sequences of protostars forming from massive cores. Each evolutionary track was built from three initial conditions: clump mass surface density Σ_{cl}, core mass M_c, and core rotational-to-gravitational energy ratio β_c. Extending this model to low-mass star formation, low-mass cores have radii $R_c = 3.3 \times 10^{-2}$ pc $(M_c/2\ M_\odot)^{1/2}(\Sigma_{cl}/0.1\ \mathrm{g\ cm}^{-2})^{-1/2}$. Note that Σ_{cl} enters this formula because it sets the core surface pressure via $P \simeq 0.88 G \Sigma_{cl}^2$. In a Taurus-like region with $\Sigma_{cl} \sim 0.03$ g cm^{-2}, the typical radius of a 2 $M_\odot$ core (which will form a $\sim$1 $M_\odot$ star if the efficiency $\sim$0.5) is $\sim$0.06 pc. In an Orion-like region with $\Sigma_{cl} \sim 0.3$ g cm^{-2}, this core has $R_c \sim 0.02$ pc, consistent with the observed prestellar cores in these regions (Ward-Thompson et al. 2007). The core is assumed to be a singular polytropic sphere at the start of collapse, with a power-law density distribution $\rho \propto r^{-k_\rho}$ with $k_\rho = 1.5$.

Collapse follows inside-out expansion wave solutions (McLaughlin & Pudritz 1997) expected of singular polytropic cores. In later non-homologous stages after the expansion wave reaches the core boundary, we simply lower the envelope density while fixing the density profile shape and outer boundary, normalizing to the remaining envelope mass. Inside the sonic point, we apply the Ulrich (1976) solution for density and velocity profiles to model infall with rotation, which conserves angular momentum. The disk is described by an α-

disk model, including the effects of outflow and accretion infall (ZTM13). The disk mass is set equal to 1/3 of the stellar mass, which is expected if self-gravity is regulating accretion and angular momentum transport. The disk outer radius is set by the centrifugal radius, increasing with protostellar growth as $r_d = 84$ AU $(\beta_c/0.02)(M_{*d}/m_{*d})(M_{*d}/M_c)^{2/3}(R_c/0.03\ \mathrm{pc})$ (ZTH14), where m_{*d} is the star+disk mass and M_{*d} is the idealized star+disk mass in the case of no outflow feedback, making m_{*d}/M_{*d} the average star formation efficiency. This assumes angular momentum is conserved inside the sonic point. The disk could be smaller if the magnetic braking was relatively strong (Li et al. 2014).

Bipolar protostellar outflows carve out low-density cavities, which gradually widen, affecting how the envelope is irradiated by the protostar. We include this process by considering when enough wind momentum is accumulated to accelerate the envelope material to the escape velocity (Matzner & McKee 2000; ZTH14). We assume an outflow momentum distribution with polar angle $\dot{p} \propto 1/\sin^2 \theta$, suitable for X-winds or disk winds at large distances (Matzner & McKee 1999). Concentration of wind momentum toward $\theta = 0°$ implies that outflow breakout first occurs at the poles and then gradually widens. The outflowing mass rate is assumed to be 0.1 $\dot{m}_*$, typical for disk winds (Königl & Pudritz 2000). After the opening angle is determined, we carve out such cavities from the envelope, but with detailed wall shapes set to follow inflowing Ulrich streamlines for simplicity. We fill the cavities with dust and gas distributions from a disk wind solution (Blandford & Payne 1982; ZTM13).
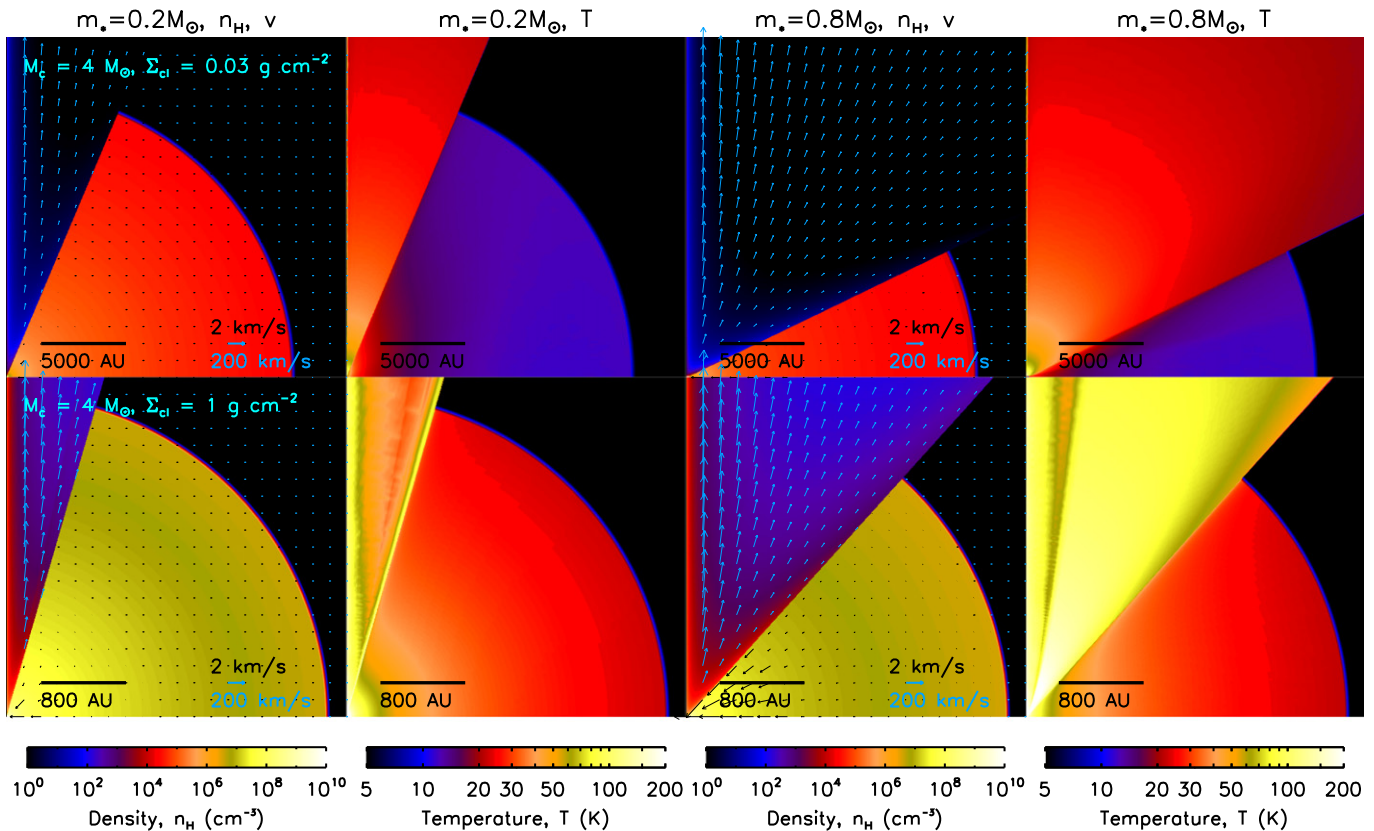
Figure 2. RT simulation input density profiles (1st/3rd columns) and converged temperature profiles (2nd/4th columns) for $M_c = 4\,M_\odot$ cores at $m_* = 0.2\,M_\odot$ (1st/2nd columns) and $m_* = 0.8\,M_\odot$ (3rd/4th columns) for $\Sigma_{cl} = 0.03$ g cm^{-2} (top row) and $\Sigma_{cl} = 1$ g cm^{-2} (bottom row). In each panel, protostar is at the lower left, the x-axis follows the disk midplane, and the y-axis follows the outflow/rotation axis. Note that upper and lower rows have different size scales. Blue/black arrows show outflow/inflow velocity fields, with different scales.

Protostellar evolution, i.e., the internal structure, size, and luminosity, is calculated with a multi-zone numerical model (Hosokawa & Omukai 2009; Hosokawa et al. 2010) with an accretion rate regulated by gradually widening outflow feedback (ZTH14). Half the accretion energy ($Gm_* \dot{m}_*/2r_*$) is released from the disk, partly radiated ($L_{acc,disk}$) and partly driving the disk wind. The other half is radiated from the boundary layer where the accretion flow hits the protostellar surface ($L_{acc,bdl}$). The total luminosity from the source is therefore $L_{tot} = L_* + L_{acc,bdl} + L_{acc,disk}$.

Thus, we self-consistently model core collapse and rotation, disk growth, outflow cavity widening, and protostar evolution, based on three initial conditions Σ_{cl}, M_c, and β_c. We assume typical $\beta_c = 0.02$ from observations of low-mass prestellar cores (Goodman et al. 1993). β_c affects the disk size and shape of rotating inflow streamlines, which, although influencing the temperatures of inflowing gas near the disk, do not affect the envelope temperature as significantly as Σ_{cl}. Therefore, we defer an exploration of β_c variation to a future study. We choose $\Sigma_{cl} = 0.03,\ 0.1,\ 0.3,\ 1$ g cm^{-2}, mimicking environments from Taurus-like regions to IRDCs/GC. We set $M_c = 2,\ 3,\ 4\,M_\odot$ to form a small model grid.

For each initial condition, we sample $\gtrsim 100$ stages evenly distributed in time to construct an evolutionary sequence. The first steps start with protostars of $m_* \sim 0.01\,M_\odot$ and $L_* \sim 0.001\,L_\odot$. However, depending on Σ_{cl}, initial accretion luminosities vary greatly, so total stellar+accretion luminosities range from $\sim 0.1 - 5\,L_\odot$. At each time step we simulate continuum RT using the Monte Carlo code HOCHUNK3D

(Whitney et al. 2013) to calculate temperature profiles. The simulations use a 3D grid starting from the stellar surface and covering the whole core. The disk is typically covered by $\sim 1/3 - 1/2$ of the total radial grid of 1000 zones (finer spacing in the inner disk). Four dust opacity types are used in the envelope, high density disk, low-density disk, and outflow cavity regions (see ZT11 for details). Envelope and disk dust grains have ice mantles; outflow cavity grains are bare. A gas-to-dust mass ratio of 100 is used throughout. Photons comprising the total $L_* + L_{acc,bdl}$ are radiated isotropically from the stellar surface following the blackbody spectrum of temperature $T_{*,bdl} = [(L_* + L_{acc,bdl})/4\pi\sigma r_*^2]^{1/4}$. Photons comprising the total $L_{acc,disk}$ are launched from the disk with an α-disk radial dependence and a Gaussian vertical distribution (ZTM13).

We include external illumination of a standard solar neighborhood interstellar radiation field (ISRF) attenuated by clump extinction of given Σ_{cl}. This may underestimate external illumination in some cases like the GC, where ISRF can be $\sim 1000\times$ greater (Clark et al. 2013), though high Σ_{cl} and clump extinction counteract this. In Orion-like regions, massive young stars may strongly increase the external illumination of cores. Higher external illumination in such high Σ_{cl} regions would further amplify the contrast of the temperatures of protostellar cores in the low and high Σ_{cl} environments. Our adopted external illumination sets a lower limit for the earliest stage core temperature, ~ 10 K.

At each time step, spectral energy distributions (SEDs) and IR continuum images are calculated from the input density and
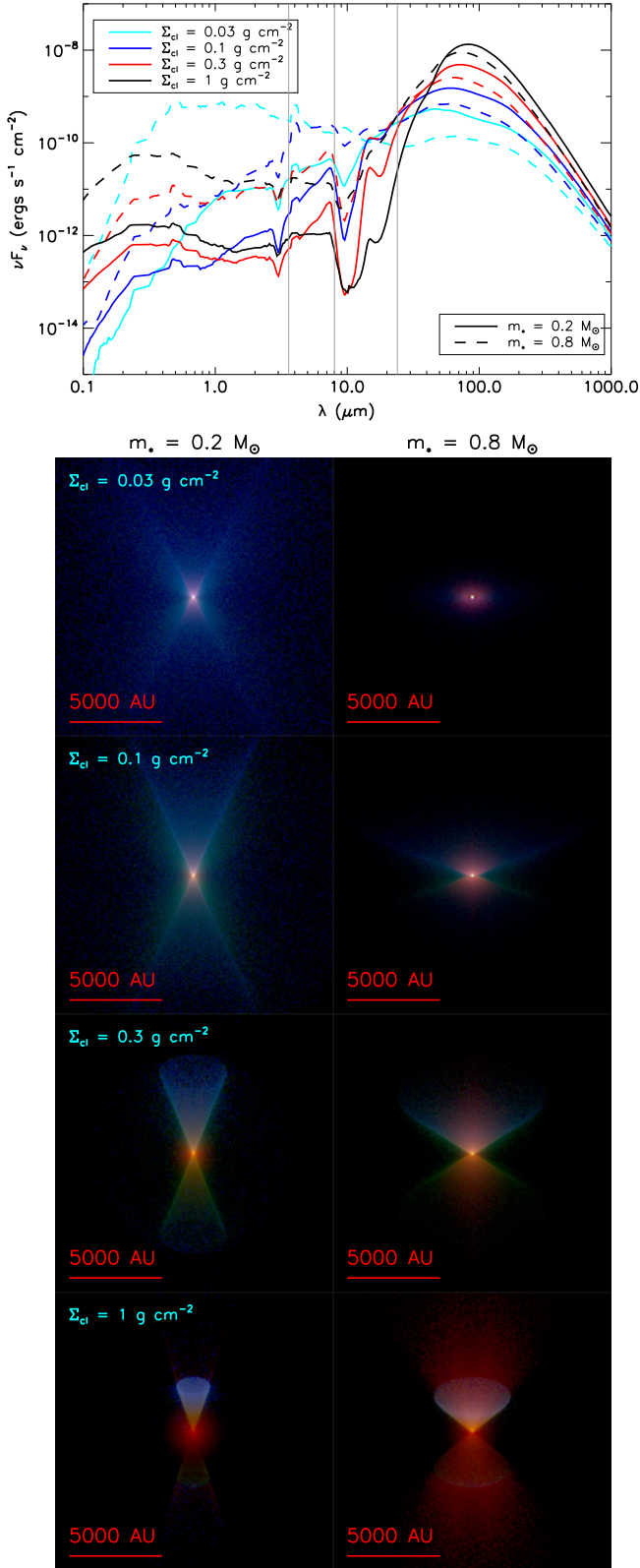
Figure 3. SEDs and three-color images (blue/green/red: 3.6/8/24 μm) for $M_c = 4\,M_\odot$ cores viewed at 500 pc distance and 60° inclination angle between the line of sight and outflow axis with $m_* = 0.2\,M_\odot$ (left) and $m_* = 0.8\,M_\odot$ (right) for $\Sigma_{cl} = 0.03$, 0.1, 0.3, 1 g cm^{-2} (top to bottom rows). One color stretch is used for $m_* = 0.2\,M_\odot$ models, another for $m_* = 0.8\,M_\odot$ models, so a relative color comparison should be made only for models at the same evolutionary stage.

converged temperature profiles. From the velocity field we can also track material parcels from any initial core position following infall streamlines, and calculate the temperature and density evolution of that parcel ($T(t)$, $\rho(t)$) needed for further chemical modeling.

Given CO's important role in studying molecular clouds and in astrochemistry, we focus on modeling CO depletion as an example of the effect of a star-forming environment on chemical evolution. We consider CO depletion onto dust grains, thermal desorption, and cosmic ray (CR) desorption. We adopt timescales for depletion (τ_{on}) and thermal desorption ($\tau_{off,th}$) from Visser et al. (2009; Equations (35) and (36)) for grains with radii of 0.1 μm and abundances of 10^{-12} relative to H nuclei, and unity sticking efficiency. For such grains, the depletion timescale is $\tau_{on} \simeq 10^4$ yr $(n_H/10^5\ \mathrm{cm}^{-3})^{-1}$ $(T/20\ \mathrm{K})^{-1/2}$, and the thermal desorption timescale is $\tau_{off,th} \simeq 3 \times 10^4$ yr $[\exp{(20\ \mathrm{K}\ /T - 1)}]^{55}$. For the latter, we also assume the energy of CO binding onto grain ice mantles to be $E_{CO} = 1100$ K, suitable for an ice surface of H_2O and CO with an abundance ratio of 30. The CR desorption timescale ($\tau_{off,CR}$) is from Keto & Caselli (2008; Equation (11); see also Hasegawa & Herbst 1993). For the same grains and assuming a CR ionization rate of 3×10^{-17} s^{-1}, $\tau_{off,CR} \simeq 2 \times 10^5$ yr, independent of temperature and density. Note that in a magnetized core/clump, CRs may be absorbed or mirrored, lowering ionization rates by factors of $\sim 2-4$ (Padovani & Galli 2011), thus increasing $\tau_{off,CR}$ by the same factor.

The evolution of relative gas-phase CO abundance (CO_{gas}) is then described via $dCO_{gas}/dt = -CO_{gas}/\tau_{on}+(1 - CO_{gas})/\tau_{off,th}+(1 - CO_{gas})/\tau_{off,CR}$. The shortest timescale among the three processes is at most $\sim 10^4$ yr, much shorter than the star formation or free-fall timescale, $\sim 10^5$ yr in the fastest collapse (highest Σ_{cl}) model. So, typically we can assume the equilibrium value for CO_{gas}, calculated as $CO_{gas} = (\tau_{on}\tau_{off,th} + \tau_{on}\tau_{off,CR})/ (\tau_{on}\tau_{off,th}+\tau_{on}\tau_{off,CR}+\tau_{off,th}\tau_{off,CR})$. Note that $\tau_{off,th}$ is very temperature-sensitive. Below ~ 20 K, $\tau_{off,th}$ is so long that it is unimportant and CO depletion is determined by the other two processes, $CO_{gas} \simeq \tau_{on}/(\tau_{on} + \tau_{off,CR})$. In this case, higher temperature and density lead to shorter τ_{on} and lower gas-phase CO abundance (higher depletion factor), but the dependence is weak ($\tau_{on} \sim n_H^{-1}T^{-1/2}$). When the temperature reaches $\gtrsim 20$ K, $\tau_{off,th}$ drops very quickly and becomes much shorter than the other two processes, leading to $CO_{gas} \simeq 1$, i.e., most CO molecules are in the gas phase. The depletion factor is defined as $f_D \equiv 1/CO_{gas}$. Note that we always assume the same temperature for dust and gas, valid for $n_H \gtrsim 10^5$ cm^{-3} (Doty & Neufeld 1997), which is true for envelopes in most models, except the outer envelope in the $\Sigma_{cl} = 0.03$ g cm^{-2} case. Here we expect slightly higher dust than gas temperatures because of dust absorption of IR radiation. Then, τ_{on} becomes longer. Dust and gas temperature coupling is even weaker in the outflow cavities, but CO is expected to be mostly in the gas phase, and here we are focusing on the envelope.

3. RESULTS

Figure 1 shows the evolution of instantaneous star formation efficiency (ϵ_*), protostellar accretion rate, and total luminosity in models with different Σ_{cl} and M_c. Here, $\epsilon_* \equiv \dot{m}_*/\dot{M}_{*d}$ with $\dot{m}_*$ being the protostellar accretion rate and $\dot{M}_{*d}$ being the idealized mass growth rate of the star+disk in the absence of
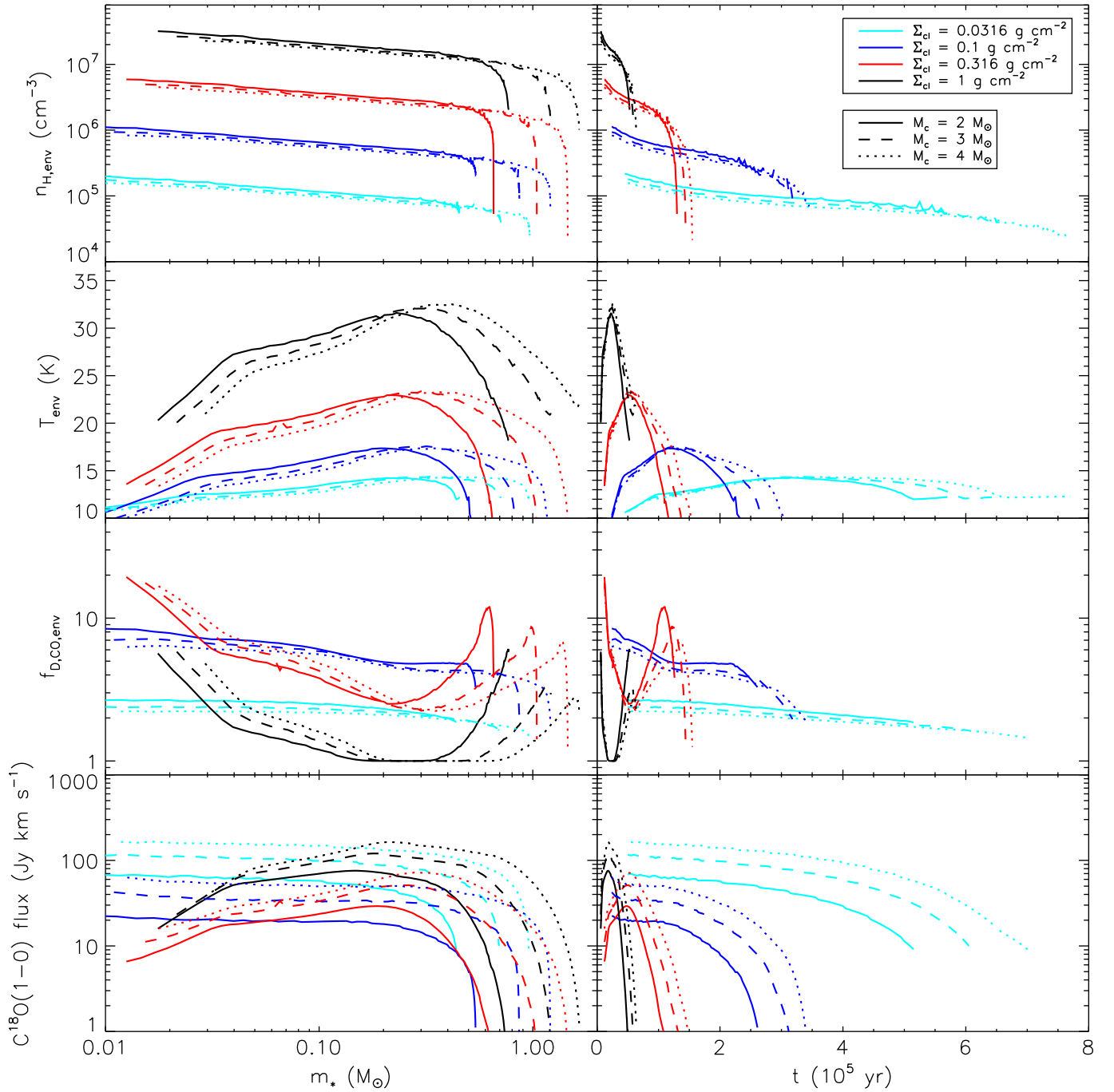
Figure 4. Evolution of envelope mass-weighted mean density (top row), mean temperature (T_{env}; 2nd row), CO depletion factor ($f_{D,CO,env} = M_{CO,env}/M_{CO,gas,env}$; 3rd row), and $C^{18}O(J = 1-0)$ flux (bottom row) with stellar mass (left) and time (right) for models with various Σ_{cl} and M_c. The $C^{18}O$ abundance is calculated from $[^{12}CO]/[H_2] = 10^{-4}$ (Frerking et al. 1982), $[^{12}CO]/[C^{13}O] = 62$ (Langer & Penzias 1993), and $[^{13}CO]/[C^{18}O] = 5.5$ (Wilson & Matteucii 1992).

outflow feedback. As the protostar grows, gradual opening up of outflow cavities causes ϵ_* to drop. Such feedback curtails the power-law growth of $\dot{m}_*$ with m_* (expected for collapse of the adopted singular polytropic core). This accretion rate drop marks the end of the main accretion phase and the start of the core clearing phase (defined as $m_* = M_{env}$). During the whole evolutionary track, the accretion luminosity significantly exceeds the intrinsic internal stellar luminosity, so the total luminosity closely tracks accretion rate evolution, except for minor features due protostellar radius evolution. We see that both the accretion rate and luminosity depend sensitively on

Σ_{cl}, but less so on M_c. In the highest pressure $\Sigma_{cl} = 1$ g cm^{-2} environments, the accretion rate and luminosity can be $10\times$ higher than in the $\Sigma_{cl} = 0.03$ g cm^{-2} environment. The star formation timescale is also sensitive to Σ_{cl}, being much shorter in a high Σ_{cl} environment, since $t_{*f} \propto M_c^{1/4}\Sigma_{cl}^{-3/4}$ (McKee & Tan 2003). For a core with a given initial mass, the final stellar mass also depends on Σ_{cl}, with a more massive star (i.e., higher star formation efficiency) being formed at higher Σ_{cl}. This is because it is more difficult for outflows to break out and widen in a denser core.
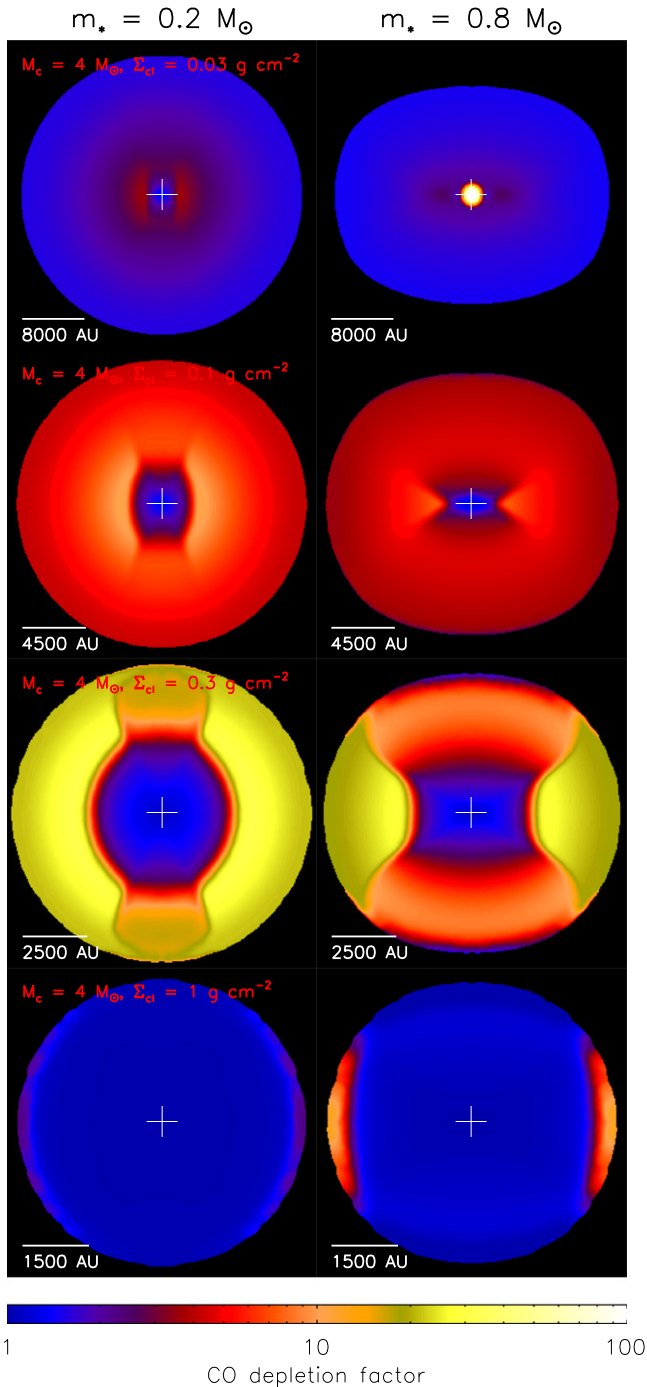
Figure 5. CO depletion factor maps ($f_{D,CO}$) for $M_c = 4\,M_\odot$ cores viewed at 60° inclination angle between the line of sight and outflow axis with $m_* = 0.2\,M_\odot$ (left) and $m_* = 0.8\,M_\odot$ (right) for $\Sigma_{cl} = 0.03, 0.1, 0.3, 1\,\mathrm{g\,cm^{-2}}$ (top to bottom rows; note the varying size scales).

Figure 2 shows examples of input density profiles for the RT simulation and resultant temperature profiles at selected stages ($m_8 = 0.2, 0.8\,M_\odot$) in two models with different $\Sigma_{cl} = 0.03, 1\,\mathrm{g\,cm^{-2}}$, chosen to illustrate the extremes of the explored range. Although the ambient clump is important for setting core properties, it is not included explicitly in our RT simulation (i.e., assumed empty outside the core boundary), given the extra parameters needed to describe the clump

density structure. This may lead to a modest underestimation of core temperatures due to back heating from the clump. In both cases, following the evolutionary sequences, we see that outflow cavities widen and core envelopes are being heated up due to increasing luminosities (from 70 to 80 $L_\odot$ in the low Σ_{cl} case; from 160 to 390 $L_\odot$ in the high Σ_{cl} case). At the same m_*, the core is much more compact and denser for high than for low Σ_{cl}. The outflow opening angle is also smaller in the high Σ_{cl} case. Envelope temperatures in this case reach ~20–30 K, significantly warmer than in the low Σ_{cl} case, which is $\lesssim$15 K.

Figure 3 shows simulated SEDs and Spitzer 3.6, 8, 24 μm three-color images at the same two evolutionary stages for models with $M_c = 4\,M_\odot$ but four different Σ_{cl} values. For a core with a given initial mass and at the same m_* from low to high Σ_{cl} environments, the far-IR (FIR) SED peak becomes higher and moves to longer wavelengths due to higher luminosity and higher envelope extinction. Higher extinctions also suppress short wavelength fluxes, making the MIR slope steeper than in low Σ_{cl} environments. IR morphology is also strongly affected by Σ_{cl}. For low Σ_{cl}, emission is dominated by the central source and the innermost regions of the envelope and outflow cavity walls. Outflow cavities become the dominant feature as Σ_{cl} increases. Due to higher extinction of the envelope at higher Σ_{cl}, the contrast of near- and far-facing outflow cavities becomes higher than for lower Σ_{cl}s. The source also appears redder in higher Σ_{cl} environments. As the protostar evolves, shorter wavelength fluxes increase while the FIR peak decreases, which agrees with the transition from Class 0 to Class I sources (André 1995). Outflow cavity widening can be clearly seen from IR morphologies. Due to larger outflow cavities and less dense envelopes, the emission becomes more peaked toward the central source in later stages.

A quantitative dependence of core density and temperature on Σ_{cl} is shown in the first two rows of Figure 4. Both mass-weighted mean density and temperature are highly dependent on Σ_{cl}, but less affected by M_c. Cores in higher Σ_{cl} environments are denser and warmer. In the highest Σ_{cl} environment the envelope mean temperature reaches ~30 K, while for low Σ_{cl} the mean temperature is always between 10 and 15 K. Potential crowding of stars in high Σ_{cl} environments could make the external illumination significantly higher than the standard ISRF, which would make the envelope even warmer than estimated here, amplifying the contrast between these environments. Note that in a high Σ_{cl} environment the star formation timescale is much shorter, so material stays in a warmer state for a shorter time, while in the low Σ_{cl} environment it stays in a cooler state for a longer time. For each evolutionary track, the envelope density decreases as a power law, as expected for a collapsing polytropic sphere, and quickly decreases in the late stages after the expansion wave reaches the core boundary and self-similarity breaks down. The temperature evolution shows an increase at first and then a drop, mainly due to the increase and decrease in accretion rate and thus luminosity. Outflow cavity widening also contributes to the increase in envelope temperature, as a wider cavity facilitates irradiation by the protostar.

Average envelope CO depletion factors, $f_{D,CO,env}$, are shown in the third row of Figure 4, determined by the balance between depletion of molecules onto dust grains and thermal or CR desorption. When $T \gtrsim 20$ K, thermal desorption is much faster than the other two processes, leading to very low CO depletion. Thus, models with the highest Σ_{cl} have the lowest f_D. When

$T \lesssim 20$ K, thermal desorption becomes much slower and CO depletion is determined by the other two processes. Since the CR desorption timescale is independent of temperature and density, while the depletion timescale scales as $\tau_{on} \simeq n_H^{-1} T^{-1/2}$, CO is more depleted when temperature and density are higher. Therefore models with the lowest Σ_{cl}, which have lower densities and temperatures, also have relatively low $f_{D,CO,env}$. The two intermediate cases with $\Sigma_{cl} = 0.1, 0.3$ g cm^{-2} have relatively high CO depletion. In models with lower surface densities ($\Sigma_{cl} = 0.03, 0.1$ g cm^{-2}) the mean envelope temperature is always $\lesssim 15$ K and $f_{D,CO,env}$ does not vary much during the evolution, since the depletion timescale is only weakly dependent on temperature and density. In the two higher surface density environments, CO depletion drops faster at first as the temperature gradually increases to ~ 20 K, and then increases again as the envelope cools down. CO depletion drops at the end of the evolutionary tracks as the density quickly declines. CO depletion is not as sensitive to core mass. These different behaviors of CO depletion affect line fluxes of CO and its isotopologues, as shown in the fourth row of Figure 4. For cores with the same mass, C^{18}O line emission (assumed to be optically thin) is stronger in an environment with either very high or very low Σ_{cl}, but lower in intermediate environments. Variation can be a factor of ~ 5 between cores in different environments.

Figure 5 shows simulated CO depletion factor maps of cores in different Σ_{cl} environments at the two fiducial evolutionary stages. As discussed above, from $\Sigma_{cl} = 0.03$ to 0.3 g cm^{-2}, as Σ_{cl} increases, $f_{D,CO}$ increases because higher core temperatures and densities in higher Σ_{cl} environments shorten the depletion timescale. However, near the protostar depletion is low where $T \gtrsim 20$ K causes thermal desorption timescales to be shorter than depletion timescales. For the highest $\Sigma_{cl} = 1$ g cm^{-2} almost all of the envelope becomes warm enough for efficient thermal desorption and low $f_{D,CO}$. Therefore, at both extremes of high and low Σ_{cl} environments, we expect smooth distributions of low CO depletion factor over the protostellar core, but in environments with intermediate $\Sigma_{cl} \sim 0.1$–0.3 g cm^{-2}, we expect higher CO depletion toward the outer core and a low CO depletion hole toward the center. Such distributions of $f_{D,CO}$ may be tested observationally.

4. CONCLUSIONS

We investigated how mass surface densities, Σ_{cl}, of star-forming regions affect thermal and chemical evolution of protostellar cores, with implications for infrared morphologies and CO depletion. In high Σ_{cl} high-pressure environments, cores of a given mass are more compact, denser, and collapse with higher accretion rates, forming more luminous protostars with higher efficiencies that lead to warmer infall envelopes. When $\Sigma_{cl} = 0.03$ g cm^{-2}, the mean temperature is ~ 10–15 K. It rises to ~ 25–30 K in the highest $\Sigma_{cl} = 1$ g cm^{-2} case. As Σ_{cl} increases, infrared morphologies reveal more dominant outflow cavities that show greater asymmetry between near- and far-facing sides. CO depletion factors are small at low Σ_{cl} since cores have low densities, leading to low rates of adhesion of molecules to dust. $f_{D,CO}$ rises at intermediate Σ_{cl} as cores become denser, but there is a central warm $\gtrsim 20$ K low-

depletion region. This grows for more luminous protostars, and for the high $\Sigma_{cl} \sim 1$ g cm^{-2} case it encompasses the entire core envelope over most of the evolution.

Further implications of these models on disk structure and possible fragmentation for binary formation (Kratter et al. 2010), with fragmentation via gravitational instability being easier in larger, cooler disks, more general astrochemical evolution (Visser et al. 2011) in the infall envelope and disk, and for dust grain coagulation in these phases (Birnstiel et al. 2012), remain to be investigated in future studies.

REFERENCES

André, P. 1995, Ap&SS, 224, 29
Battersby, C., Ginsburg, A., Bally, J., et al. 2014, ApJ, 787, 113
Birnstiel, T., Klahr, H., & Ercolano, B. 2012, A&A, 539, 148
Blandford, R. D., & Payne, D. G. 1982, MNRAS, 199, 883
Bonnell, I. A., Bate, M. R., Clarke, C. J., & Pringle, J. E. 2001, MNRAS, 323, 785
Butler, M. J., & Tan, J. C. 2012, ApJ, 754, 5
Clark, P. C., Glover, S. C. O., Ragan, S. E., Shetty, R., & Klessen, R. S. 2013, ApJL, 768, L34
Doty, S. D., & Neufeld, D. A. 1997, ApJ, 489, 122
Elmegreen, B., Hurst, R., & Koenig, X. 2014, ApJL, 782, L1
Frerking, M. A., Langer, W. D., & Wilson, R. W. 1982, ApJ, 262, 590
Hincelin, U., Wakelam, V., Commercon, B., Hersant, F., & Guilloteau, S. 2013, ApJ, 775, 44
Goodman, A. A., Benson, P. J., Fuller, G. A., & Myers, P. C. 1993, ApJ, 406, 528
Hasegawa, T., & Herbst, E. 1993, MNRAS, 261, 83
Hosokawa, T., & Omukai, K. 2009, ApJ, 691, 823
Hosokawa, T., Yorke, H. W., & Omukai, K. 2010, ApJ, 721, 478
Keto, E., & Caselli, P. 2008, ApJ, 683, 238
Königl, A., & Pudritz, R. E. 2000, in Protostars and Planets IV, ed. V. Mannings (Tucson, AZ: Univ. Arizona Press), 759
Kratter, K. M., Matzner, C. D., Krumholz, M. R., & Klein, R. I. 2010, ApJ, 708, 1585
Kryukova, E., Megeath, S. T., Hora, J. L., et al. 2014, AJ, 148, 11
Langer, W. D., & Penzias, A. A. 1993, ApJ, 408, 539
Li, Z.-Y., Banerjee, R., Pudritz, R. E., et al. 2014, in Protostars and Planets VI, ed. H. Beuther et al. (Tucson, AZ: Univ. Arizona Press), 173
Matzner, C. D., & McKee, C. F. 1999, ApJL, 526, L109
Matzner, C. D., & McKee, C. F. 2000, ApJ, 545, 364
McKee, C. F., & Tan, J. C. 2003, ApJ, 585, 850
McLaughlin, D. E., & Pudritz, R. E. 1997, ApJ, 476, 750
Onishi, T., Mizuno, A., Kawamura, A., Ogawa, H., & Fukui, Y. 1996, ApJ, 465, 815
Padovani, M., & Galli, D. 2011, A&A, 530, 109
Plume, R., Jaffe, D. T., Evans, N. J., Martin-Pintado, J., & Gomez-Gonzalez, J. 1997, ApJ, 476, 730
Rathborne, J. M., Longmore, S. N., Jackson, J. M., et al. 2014, ApJ, 786, 140
Robitaille, T. P., Whitney, B. A., Indebetouw, R., Wood, K., & Denzmore, P. 2006, ApJS, 167, 256
Tan, J. C., Beltran, M. T., Caselli, P., et al. 2014, in Protostars and Planets VI, ed. H. Beuther et al. (Tucson, AZ: Univ. Arizona Press), 149
Ulrich, R. K. 1976, ApJ, 210, 377
Visser, R., Doty, S. D., & van Dishoeck, E. F. 2011, A&A, 534, A132
Visser, R., van Dishoeck, E. F., Doty, S. D., & Dullemond, C. P. 2009, A&A, 495, 881
Ward-Thompson, D., Andre, P., Crutcher, R., et al. 2007, in Protostars and Planets V, ed. B. Reipurth, D. Jewitt, & K. Keil., (Tucson, AZ: Univ. Arizona Press), 33
Whitney, B. A., Robitaille, T. P., Bjorkman, J. E., et al. 2013, ApJS, 207, 30
Wilson, T. L., & Matteucii, F. 1992, A&ARv, 4, 1
Zhang, Y., & Tan, J. C. 2011, ApJ, 733, 55 (ZT11)
Zhang, Y., Tan, J. C., & Hosokawa, T. 2014, ApJ, 788, 166 (ZTH14)
Zhang, Y., Tan, J. C., & McKee, C. F. 2013, ApJ, 766, 86 (ZTM13)